Astronomy & Astrophysics manuscript no.
(will be inserted by hand later)

Observations of Mira stars with the IOTA/FLUOR interferometer and comparison with Mira star models ⋆

K.-H. Hofmann[1], U. Beckmann[1], T. Blöcker[1], V. Coudé du Foresto[2], M. Lacasse[3], B. Mennesson[2], R. Millan-Gabet[3], S. Morel[3], G. Perrin[2], B. Pras[3], C. Ruilier[2], D. Schertl[1], M. Scholz[4], V. Shenavrin[5], W. Traub[3], G. Weigelt[1], M. Wittkowski[1], B. Yudin[5]

[1] Max-Planck-Institut für Radioastronomie, Auf dem Hügel 69, 53121 Bonn, Germany
[2] Observatoire de Paris-Meudon, 5 place Jules Janssen, 92195 Meudon Cedex, France
[3] Harvard-Smithsonian Center for Astrophysics, 60 Garden Street, Cambridge, Massachusetts 02138, USA
[4] Institut für Theoretische Astrophysik der Universität Heidelberg, Tiergartenstr. 15, 69121 Heidelberg, Germany, Chatterton Department of Astronomy, School of Physics, University of Sydney NSW 2006, Australia
[5] Sternberg Astronomical Institute, Universitetskii pr. 13, 119899 Moscow, Russia.

....; accepted date

Abstract. We present K'-band observations of five Mira stars with the IOTA interferometer. The interferograms were obtained with the FLUOR fiber optics beam combiner which provides high-accuracy visibility measurements in spite of time-variable atmospheric conditions. For the M-type Miras X Oph, R Aql, RU Her, R Ser, and the C-type Mira V CrB we derived the uniform-disk diameters 11.7 mas, 10.9 mas, 8.4 mas, 8.1 mas, and 7.9 mas (±0.3 mas), respectively. Simultaneous photometric observations yielded the bolometric fluxes. The derived angular Rosseland radii and the bolometric fluxes allowed the determination of effective temperatures. For instance, the effective temperature of R Aql was determined to be 2790 ±100 K. A Rosseland radius for R Aql of 250^{+100}_{-60} $R_\odot$ was derived from the angular Rosseland radius of 5.5 mas ±0.2 mas and the HIPPARCOS parallax of 4.73 mas ±1.19 mas. The observations were compared with theoretical Mira star models of Bessel et al. (1996) and Hofmann et al. (1998). The effective temperatures of the M-type Miras and the linear radius of R Aql indicate fundamental mode pulsation.

Key words. instrumentation: interferometers - stars: AGB and post-AGB - stars: late-type - stars: variables - stars: individual: X Oph, R Aql, RU Her, R Ser, V CrB

1. Introduction

The resolution of large optical telescopes and interferometers is high enough to resolve the stellar disk of nearby M giants, to reveal photospheric asymmetries and surface structures, and to study the dependence of the diameter on wavelength, variability phase, and cycle (see, e.g. Bonneau & Labeyrie 1973; Karovska et al. 1991; Quirrenbach et al. 1992; Haniff et al. 1995; Weigelt et al. 1996; van Belle et al. 1996; Perrin et al. 1999; Hofmann et al. 2000). Theoretical studies (e.g. Watanabe & Kodaira 1979; Scholz 1985; Bessell et al. 1989; Bessell et al. 1996; Hofmann et al. 1998) show that accurate monochromatic diameter measurements can significantly improve our understanding of M giant atmospheres. With the IOTA (= Infrared-Optical Telescope Array) interferometer a resolution of ∼9 mas can be achieved with its largest baseline of 38 m in the K-band. The IOTA interferometer is located at the Smithsonian Institution's Whipple Observatory on Mount Hopkins in Arizona. A detailed description of IOTA can be found in Carleton et al. (1994) and Traub et al. (1998). IOTA can be operated in the K-band with the FLUOR (= Fiber Linked Unit for Optical Recombination, Coudé du Foresto et al. 1997) fiber optics beam combiner. This beam combiner provides high-accuracy visibility measurements in spite of time-variable atmospheric conditions. The single-mode fibers in the beam combiner spatially filter the wavefronts corrugated by atmospheric turbulence (see Coudé du Foresto et al. 1997 and Perrin et al. 1998).

Send offprint requests to: K.-H. Hofmann (hofmann@mpifr-bonn.mpg.de)

⋆ Based on observations collected at the IOTA/FLUOR interferometer, Whipple Observatory, Mount Hopkins, Arizona.

2. Observations

The five Miras X Oph, R Aql, RU Her, R Ser, V CrB were observed with the IOTA interferometer on May 16, 17 and 18, 1999. The observations were carried out with the fiber

optics beam combiner FLUOR in the K'-band and with 38 m baseline (maximum baseline of the IOTA interferometer). First results have been presented at the SPIE conference *Interferometry in Optical Astronomy* (Hofmann et al. 2000). The interferograms were scanned by the delay line during the coherence time of the atmosphere. The OPD length of the scan was $\sim 100\,\mu$m (OPD = Optical Path Difference). Approximately 100 scans per baseline were recorded.

Several reference stars (Table 1) were observed for the calibration of the observations. The calibrated visibilties of the five Miras were obtained with the FLUOR data reduction software package described in Foresto et al. (1997) and Perrin et al. (1998). Fig. 1 shows the obtained visibility functions of the five Mira stars together with uniform-disk fits. The errors of the derived Mira star diameters are 2.5-3%. In Table 1 the calibrated visibilities and the derived uniform-disk diameters of the five Miras are listed, together with observational parameters (spectral type, variability period P, date of observation, variability phase $\Phi_{\rm vis}$ in visual light, projected baseline length $B_{\rm p}$, calibrated visibilities V, derived uniform-disk diameters $\Theta_{\rm UD}$, and the HIPPARCOS numbers of the reference stars).

2.1. Calibrated visibilities, stellar diameters, errors

The transfer function of the whole instrument at the time of the observation of the object was derived from visibility measurements of several reference stars (2 to 4 different reference stars per object) before and after the object observations. Indirect estimates of the diameter of reference stars had to be used, since only few stellar diameters have been measured up to now. The diameters of the reference stars were derived from the list of angular diameters for giants at K=0 according to Dyck et al. (1996). The accuracy of the estimated diameters of the reference stars is 10%. The transfer function was directly computed as the ratio between the measured fringe contrast and the visibility of the reference star. The visibility of the reference star was derived from its uniform-disk diameter estimated by the method of Dyck et al. (1996). Note, that the errors of the target star diameter are much smaller than 10%. The error $\sigma_{\Theta_{\rm Obj}}$ of the fitted UD diameter of the target star caused by the uncertainty $\sigma_{\Theta_{\rm Ref}}$ of the diameter of the reference star is given, according to the Gaussian error propagation law, by

$$\frac{\sigma_{\Theta_{\rm Obj}}}{\Theta_{\rm Obj}} = \frac{|V(\Theta_{\rm Obj})|}{|V(\Theta_{\rm Ref})|} \cdot \frac{|\partial V(\Theta_{\rm Ref})/\partial\Theta|}{|\partial V(\Theta_{\rm Obj})/\partial\Theta|} \cdot \frac{\Theta_{\rm Ref}}{\Theta_{\rm Obj}} \cdot \frac{\sigma_{\Theta_{\rm Ref}}}{\Theta_{\rm Ref}}, \quad (1)$$

where $V(\Theta_{\rm Obj})$ and $V(\Theta_{\rm Ref})$ are the visibilities of the target and reference star, respectively. If, for example one considers R Ser, then $\Theta_{\rm Obj}$=8.10 mas, $\Theta_{\rm Ref}$=3.81 mas, $V(\Theta_{\rm Obj})$=0.55, $V(\Theta_{\rm Ref})$=0.88, $\partial V(\Theta_{\rm Obj})/\partial\Theta$=0.09 mas^{-1}, and $\partial V(\Theta_{\rm Ref})/\partial\Theta$=0.06 mas^{-1}. According to Eq.(1) the relative error of the UD diameter of the (larger) target star is 2%, while the diameter error of the reference star is 10%.

The total errors of the calibrated visibilities presented in Table 1 take into account the following errors:

- the statistical error of the raw visibility measurement in each star (e.g. photon and detector noise);
- the errors of the measured gain matrix (link between photometric and interferometric signals, Foresto et al. 1997);
- the uncertainty on the predicted visibility of the reference star (the error of the estimated diameter of the reference star was assumed to be 10% according to Dyck et al. 1996);
- the uncertainties of the transfer function at the time of the object measurement (the transfer function is interpolated between measurements of the reference star before and after the object observation; see details in Perrin et al. 1998).

In addition to the reduction based on all available reference stars, each target star was also reduced with each of the 2-4 different reference stars separately. All these calibrated visibilities are within the error bars given in Table 1.

The uniform-disk diameters and the diameters corresponding to a model center-to-limb intensity variation (hereafter CLV) were derived from the calibrated visibilities with a χ^2 fit:

$$\chi^2 = \sum_{\rm i=1}^{\rm N} \frac{|V_{\rm i} - V(\Theta, u_{\rm i})|^2}{\sigma_{\rm i}^2}, \quad (2)$$

where $V_{\rm i}$ denotes the measured visibility at spatial frequency $u_{\rm i}$ with the error $\sigma_{\rm i}$, $V(\Theta, u_{\rm i})$ is the visibility of the theoretical clv (uniform-disk or any model clv) at frequency $u_{\rm i}$ as a function of the disk diameter Θ, and N denotes the number of measured visibilities. The diameter error $\sigma_{\Theta_{\rm Obj}}$ of the fitted stellar diameter $\Theta_{\rm Obj}$ is linked, according to the Gaussian error propagation law, to the total errors $\sigma_{\rm i}$ of the derived object visibilities $V_{\rm i}$ by

$$1/\sigma^2_{\Theta_{\rm Obj}} = \sum_{\rm i=1}^{\rm N} |a_{\rm i}|^2/\sigma_{\rm i}^2, \quad (3)$$

where $a_{\rm i}$ denotes the derivative $\partial V(\Theta_{\rm Obj}, u_{\rm i})/\partial\Theta$ of the visibility of the theoretical clv at the fitted disk diameter $\Theta_{\rm Obj}$. The diameter errors listed in Table 1 and used below are derived from the above relation.

3. Comparison of the observations with Mira star models

In this section we derive angular diameters from the measured visibilities by fitting different theoretical center-to-limb intensity variations of different Mira star models (Bessel et al. 1996 = BSW96, Hofmann et al. 1998 = HSW98). From these angular diameters and the bolometric fluxes, we derive effective temperatures. For R Aql a

Table 1. Observed data of X Oph, R Aql, RU Her, R Ser and V CrB.

Star	spectral type	P [days]	Date	$\Phi_{\rm vis}$	$B_{\rm p}$ [m]	V	$\Theta_{\rm UD}$ [mas]	reference stars
X Oph	M5e-M9e	328	99 May 17	0.71	35.47	0.2317±0.024	11.74±0.30	HIP 86742
			99 May 18		34.75	0.2554±0.027		HIP 98337
			99 May 18		34.57	0.2279±0.025		HIP 98438
								HIP 97278
								HIP 97278
R Aql	M5e-M9e	284	99 May 17	0.17	35.42	0.2927±0.027	10.90±0.33	HIP 86742
			99 May 18		34.48	0.3295±0.031		HIP 98337
								HIP 98438
								HIP 97278
RU Her	M6e-M9	484	99 May 17	0.07	37.95	0.4768±0.017	8.36±0.20	HIP 71053
					37.73	0.4769±0.017		HIP 78159
R Ser	M5e-M9e	356	99 May 18	0.28	35.74	0.5467±0.016	8.10±0.20	HIP 61658
								HIP 75530
								HIP 85934
V CrB	C6,2e(N2e)	357	99 May 16	0.07	37.78	0.5288±0.017	7.86±0.24	HIP 73555
					38.02	0.5180±0.023		HIP 81833

HIPPARCOS parallax is available which allows us to determine linear radii. The comparison of these measured stellar parameters with theoretical ones indicate whether any of the models is a fair representation of the observed Mira stars.

Table 2. Properties of Mira model series (see text)

Series	Mode	P(d)	$M/M_\odot$	$L/L_\odot$	$R_{\rm p}/R_\odot$	$T_{\rm eff}$/K
D	f	330	1.0	3470	236	2900
E	o	328	1.0	6310	366	2700
P	f	332	1.0	3470	241	2860
M	f	332	1.2	3470	260	2750
O	o	320	2.0	5830	503	2250

All Mira star models used in this paper are from BSW96 (D and E series) and from HSW98 (P, M and O series). They were developed as possible representations of the prototype Mira variable o Ceti, and hence have periods P very close to the 332 day period of this star; they differ in pulsation mode, assumed mass M and assumed luminosity L; and the BSW96 models differ from the (more advanced) HSW98 models with respect to the pulsation modelling technique. The five models represent stars pulsating in the fundamental mode (f; D, P and M models) or in the first-overtone mode (o; E and O models). Table 2 lists the properties of these Mira model series ($R_{\rm p}$ = Rosseland radius of the non-pulsating "parent" star of the Mira variable [see BSW96/HSW98] , i.e. the distance from the parent star's center, at which the Rosseland optical depth $\tau_{\rm Ross}$ equals unity; $T_{\rm eff} \propto (L/R_{\rm p}^2)^{1/4}$ = effective temperature; L = luminosity). Table 3 provides the link between the 22 abscissa values (model-phase combinations m) in Figs. 2 and 3, and the models, and it additionally lists the variability phase, Rosseland and stellar K-band filter radius (definition given below) in units of the parent star radius $R_{\rm p}$, and the effective temperature. We compare predictions of these models at different phases and cycles with our measurements. Note in this context that both observations (e.g. Spinrad and Wing 1969; Tuthill et al. 1995) and models (e.g. HSW98) have shown that noticeable cycle-to-cycle variations may occur in Mira variables.

Monochromatic radius R_λ, Rosseland radius R and stellar filter radius $R_{\rm f}$. We use the conventional stellar radius definition where the monochromatic radius R_λ of a star at wavelength λ is given by the distance from the star's center at which the optical depth equals unity ($\tau_\lambda = 1$). In analogy, the photospheric stellar radius R (Rosseland radius) is given by the distance from the star's center at which the Rosseland optical depth equals unity ($\tau_{\rm Ross} = 1$). For the K-band filter used for the observations we have calculated the theoretical CLVs corresponding to the above mentioned five Mira star models at different phases and cycles. The stellar radius for filter transmission f_λ is the intensity and filter weighted radius $R_{\rm f} = \int R_\lambda\, I_\lambda\, f_\lambda\, d\lambda \,/\, \int I_\lambda\, f_\lambda\, d\lambda$, which we call stellar filter radius $R_{\rm f}$ after the definition of Scholz & Takeda (1987). In this equation R_λ denotes the above monochromatic $\tau_\lambda = 1$ radius, I_λ the central intensity spectrum and f_λ the transmission of the filter. In the K-band near-continuum window the monochromatic radius R_λ and the stellar filter radius are almost identical. Some of the models, however, predict wavelength-dependent CLV shapes within the K-

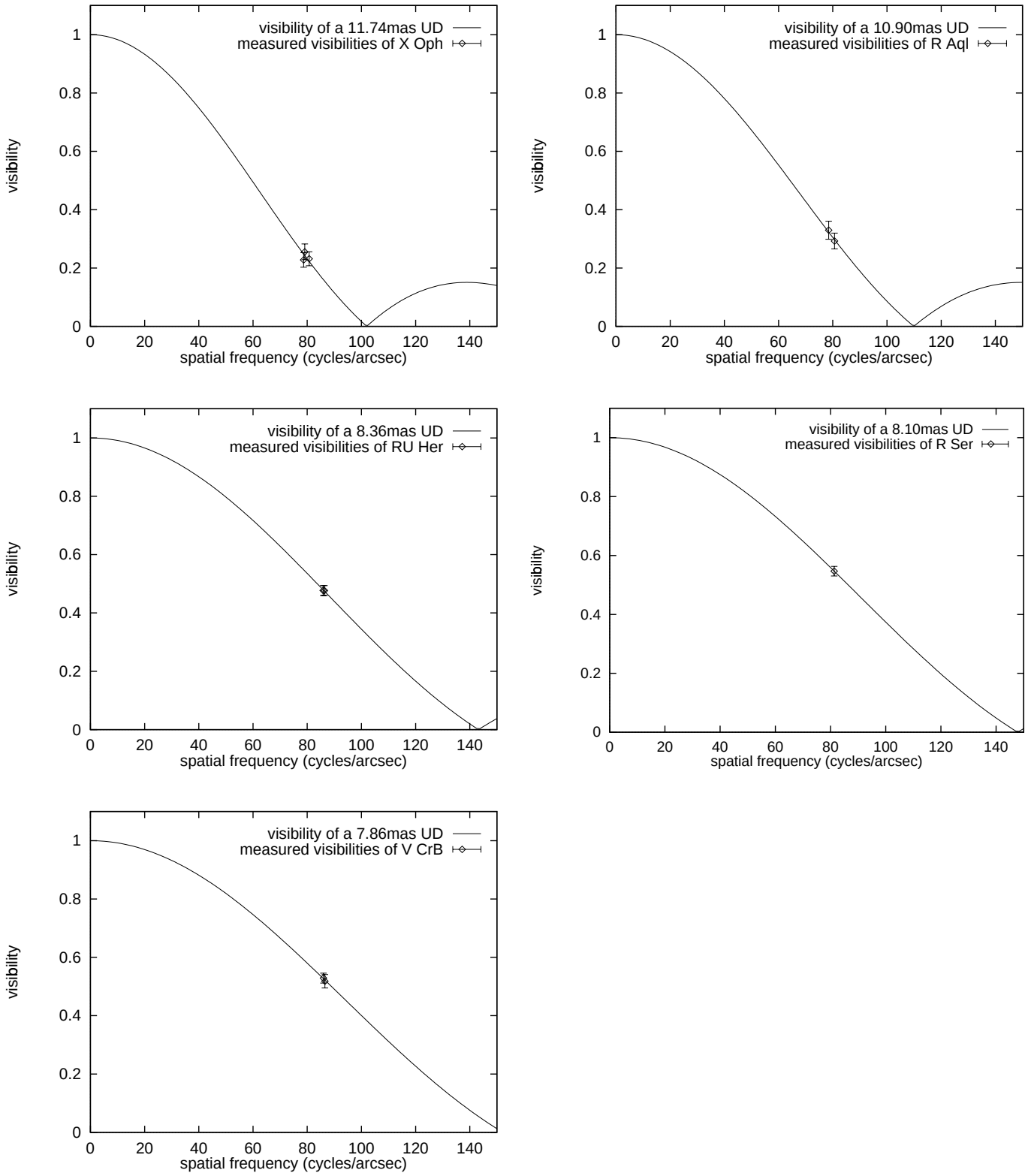

Fig. 1. Uniform-disk (UD) fits (X Oph, R Aql, RU Her, R Ser, and V CrB).

band due to molecular (mainly water) absorption, resulting in a two-component structure (i.e. disk plus tail) of the CLV (Scholz 2001, Bedding et al. 2001) and contributing to a few noticeable differences between R and $R_{\rm K}$ seen in Table 3.

Observed angular stellar K-band radius $R^a_{\rm K,m}$ *(*$a =$ *angular,* $K =$ *K-band,* $m =$ *model-phase combination) and observed angular Rosseland radius* $R^a_{\rm m}$. The observed angular stellar K-band radii $R^a_{\rm K,m}$ of the observed Miras corresponding to the model-phase combi-

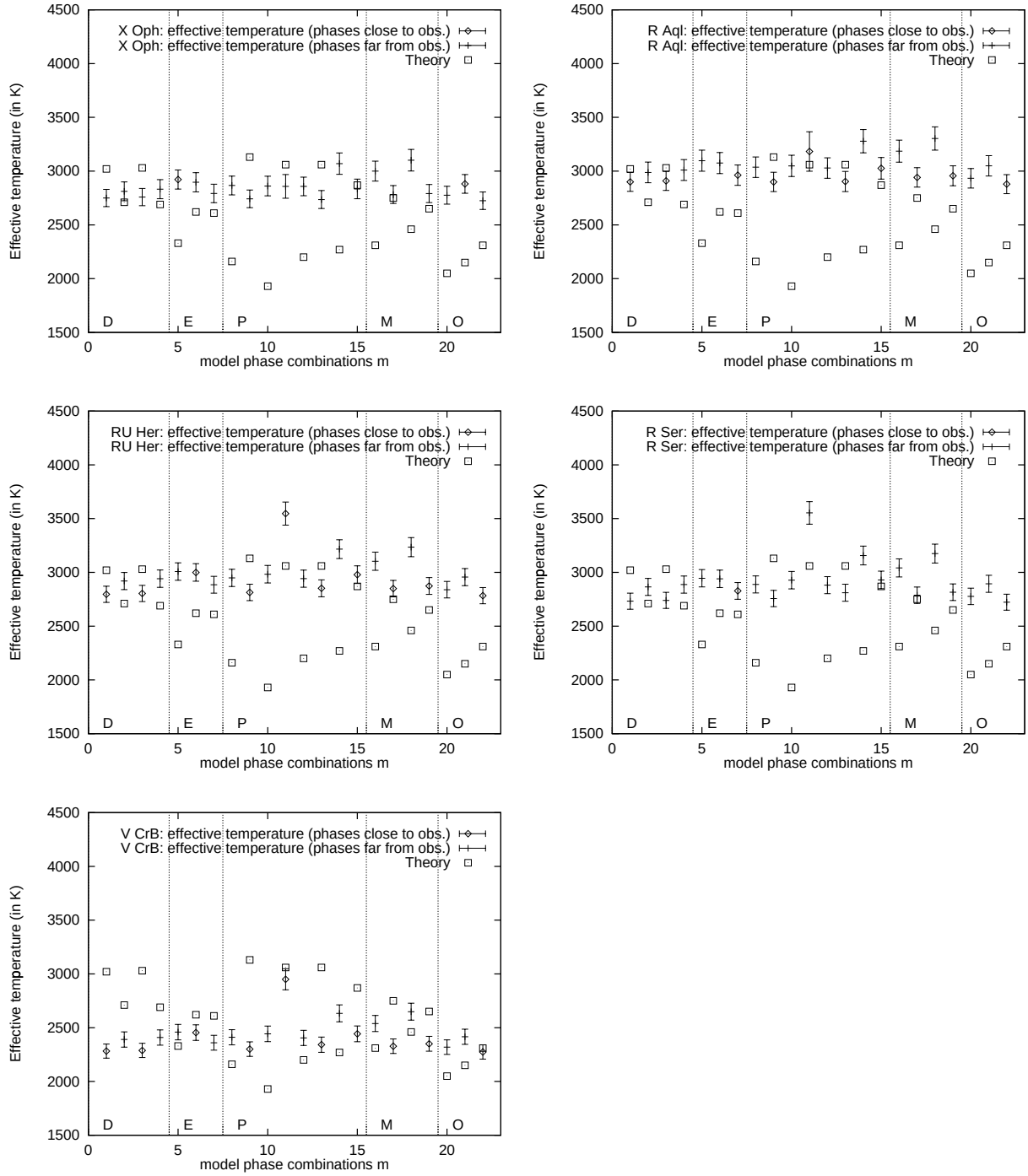

Fig. 2. Comparison of measured effective temperatures of the 5 observed Mira stars and the theoretical model effective temperatures (see text). The measured effective temperatures are derived from the angular Rosseland radii determined by least-square fits between the measured visibilities and the visibilities of the corresponding theoretical CLVs given by the models of BSW & HSW. The measured $T_{\rm eff}$ values are given with 1σ-error bars. Measured $T_{\rm eff}$ values derived from models at phases close to our observations (diamonds) and far from our observations (crosses) are shown. The theoretical model effective temperatures are plotted with squares. Table 3 shows the link between the abscissa values and the models and their phases.

nations m (see Table 3), were derived by least-squares fits between the measured visibilities and the visibilities of the corresponding theoretical CLVs. Additionally, the angular Rosseland radii $R^a_{\rm m}$ were derived from the obtained stellar K-band radii $R^a_{\rm K,m}$ and the theoretical ratios $R_{\rm m}/R_{\rm K,m}$ from Table 3 (Table 3 provides theoretical R and $R_{\rm K}$ values for each model-phase combination m). In the following subsections we apply CLVs predicted from all five models at phases both near our observations and, for comparison, also at other phases.

Table 4. Observational data and measured effective temperatures. For each star the effective temperature according to its UD diameter is listed. For R Aql and RU Her measured $T_{\rm eff}$ values are given which were derived from the Rosseland radii of those model-phase combinations where the theoretical $T_{\rm eff}$ value and the measured one are within the 2σ-error bar (see Fig. 2). The indices D, P, M refer to the pulsation models.

Star	Date	$\Phi_{\rm vis}$	K [mag]	$F_{\rm bol}$ [10^{-8} erg/cm^2 s]	$T_{\rm eff,UD}$ [K]	$T_{\rm eff,D}$ [K]	$T_{\rm eff,P}$ [K]	$T_{\rm eff,M}$ [K]
X Oph	99 May 27	0.71	-0.83	287.7±28.8	2810±90	-	-	-
R Aql	99 May 28	0.17	-0.86	305.6±30.6	2960±100	2900±90	3040±120	-
RU Her	99 May 21	0.07	-0.11	153.2±15.3	2850±80	-	2980±80	2850±80
R Ser	99 May 21	0.28	0.02	130.3±13.1	2780±80	-	-	-
V CrB	99 May 27	0.07	0.96	59.9±6.0	2320±70	-	-	-

Table 3. Link between the 22 abscissa values (model-phase combinations m) in Figs. 2 and 3, and the models. The variability phase $\Phi_{\rm vis}$ in visual light ($\Phi_{\rm vis}$ represents cycle + phase), the Rosseland radius R and the K-band radius $R_{\rm K}$ in units of the parent star radius R_p, and the effective temperature $T_{\rm eff} \propto (L/R^2)^{1/4}$ are also given.

Model	$\Phi_{\rm vis}$	$R/R_{\rm p}$	$R_{\rm K}/R_{\rm p}$	$T_{\rm eff}$/K	m
D27520	1+0.0	1.04	1.02	3020	1
D27760	1+0.5	0.91	0.90	2710	2
D28760	2+0.0	1.04	1.02	3030	3
D28960	2+0.5	0.91	0.91	2690	4
E8300	0+0.83	1.16	1.14	2330	5
E8380	1+0.0	1.09	1.10	2620	6
E8560	1+0.21	1.17	1.14	2610	7
P71800	0+0.5	1.20	1.04	2160	8
P73200	1+0.0	1.03	0.99	3130	9
P73600	1+0.5	1.49	1.12	1930	10
P74200	2+0.0	1.04	1.11	3060	11
P74600	2+0.5	1.17	1.02	2200	12
P75800	3+0.0	1.13	1.06	3060	13
P76200	3+0.5	1.13	0.96	2270	14
P77000	4+0.0	1.17	1.14	2870	15
M96400	0+0.5	0.93	0.92	2310	16
M97600	1+0.0	1.19	1.15	2750	17
M97800	1+0.5	0.88	0.90	2460	18
M98800	2+0.0	1.23	1.19	2650	19
O64210	0+0.5	1.12	1.09	2050	20
O64530	0+0.8	0.93	0.95	2150	21
O64700	1+0.0	1.05	1.01	2310	22

3.1. Effective temperature

Effective temperatures of each observed Mira star were derived from its angular Rosseland radii $R^a_{\rm m}$ and its bolometric flux using the relation

$$T_{\rm eff} = 2341\ {\rm K} \times (F_{\rm bol}/\phi^2)^{1/4} \qquad (4)$$

where $F_{\rm bol}$ is the apparent bolometric flux in units of $10^{-8}\,{\rm erg\,cm^{-2}\,s^{-1}}$ and $\phi = 2\times R^a_{\rm m}$ is the angular Rosseland diameter in mas. The bolometric fluxes were derived from optical (*VR*), near-infrared (*JHKLM*) and mid-infrared (e.g. IRAS data) photometry (see Appendix A). Interstellar extinction corrections were applied which, however, affect the fluxes only mildly (see Table A.1). The near-infrared photometry was carried out with the 1.25 m telescope at the Crimean station of the Sternberg Astronomical Institute in Moscow 12 days after our visibility observations. The V band photometry was taken from the AAVSO data base (Mattei 2001) at the time of our observations, the R band data were derived from observations with the 1.25 m telescope at the Crimean station of the Sternberg Astronomical Institute and the AAVSO data base. The conventional approximation for calculating bolometric fluxes is to use a black body function to interpolate between photometric observations in the near-infrared (*JHKLM*). However, applying only this black body as a description of the whole spectral energy distribution, yields bolometric fluxes being in most cases significantly larger than those based also on additional photometry in V and mid-infrared. In Appendix A the procedure for deriving bolometric fluxes used in this paper is described in detail. The errors of the *JHKLM* photometry do not exceed 0.03 magnitudes, whereas the errors of the V and R photometry are approx. 0.6 magnitudes which affect the bolometric fluxes. The errors of the bolometric fluxes were determined by integrating the SED derived from the photometric data at the upper and lower boundary of the error bar. The derived bolometric fluxes have errors of approx. 10%.

Fig. 2 shows a comparison of the measured and theoretical effective temperatures.

(a) For the two M stars X Oph and R Ser, the phases of the models do not fit the phases at observations (X Oph: only the E model at phase 0.83 and the O model at phase 0.80 are close to the phase 0.71 at observation; R Ser: only the E model at phase 1.21 is close to the phase 0.28 at observation).

(b) For the C-type Mira V CrB, the information drawn from Fig. 2 should be considered with due caution because the K-band continuum is slightly contaminated by molecular lines in both M and C stars, and because even the pure-continuum CLV might be influenced by the different structures of M- and C-type atmospheres. The good

description by the high-mass, first-overtone O model may be a chance match.

(c) For the remaining stars R Aql and RU Her all five models are available at phases close to the observations (phase 0.17 for R Aql and 0.07 for RU Her). Note, however, that RU Her has an appreciably longer period than the *o* Ceti period adopted for all model series. For R Aql and RU Her, phase- and model-dependent effective temperatures could be derived which are listed in Table 4.

(d) For the smaller stars RU Her and R Ser, extremely large measured effective temperatures are seen in Fig. 2 at model-phase combination m=11 (near-maximum model P74200). The P74200 model predicts a very pronounced two-component, disk-plus-tail CLV structure, as mentioned above, which essentially distorts the central maximum of the visibility of the tail-free curve at smaller spatial frequencies. For the small disks of RU Her and R Ser, the large measured visibilities (V = 0.48 and 0.55, respectively) lie in the inner portion of the central maximum which should be mostly affected by a two-component CLV structure. Obviously, such a pronounced structure is not present in these stars. For the larger disks of X Oph and R Aql, the smaller values of V = 0.23 and 0.29, respectively, belong to higher spatial frequencies at which the influence of a CLV tail, if it were present, would not be very conspicuous. Observations with several baselines would be necessary for detecting tail-generated distortions of the visibility curve.

(e) Interestingly, the visibility fit of V CrB whose disk size is similar to those of RU Her and R Ser would be compatible with a distinct two-component brightness distribution, but no model studies of limb-darkening of C-type Miras in the K bandpass are available at the present.

The four M stars X Oph, R Aql, RU Her and R Ser clearly do not fit the first-overtone models E and O. For the two M stars, R Aql and RU Her, observed at near-maximum phase, however, the measured and theoretical $T_{\rm eff}$ values are within the 2σ-error bar for some cycles of the fundamental mode models D, P and M (R Aql: all cycles of the D model and 3 of 4 cycles of the P model; RU Her: 1 of 4 cycles of the P model and 1 of 2 cycles of the M model). Table 4 lists the measured bolometric flux, the $T_{\rm eff}$ values derived from the measured UD diameter, and for the two M stars R Aql and RU Her measured $T_{\rm eff}$ values for selected models close to the phase at observation. These model-averaged $T_{\rm eff}$ values were obtained by averaging only those values where the theoretical $T_{\rm eff}$ values and the measured ones are within the 2σ-error bar. The $T_{\rm eff}$ values derived from the UD diameters are in good agreement with the model-derived effective temperatures.

3.2. Linear radii

We have derived linear stellar K-band radii $R_{\rm K,m}$ and Rosseland radii $R_{\rm m}$ of R Aql from the measured angular stellar K-band radii $R^a_{\rm K,m}$ and Rosseland radii $R^a_{\rm m}$ by using the R Aql HIPPARCOS parallax of 4.73±1.19 mas (ESA 1997, Van Leeuwen et al. 1997). The HIPPARCOS parallaxes of the other four observed Miras have too large errors to reliably estimate stellar linear radii. Fig. 3 shows the obtained linear Rosseland radii $R_{\rm m}$ and stellar K-band radii $R_{\rm K,m}$ of R Aql for all model-phase combinations m. The theoretical Rosseland radii of the D, M and P fundamental mode model series at all available near-maximum phases are close (i.e. within the error bars) to the measured Rosseland radii of R Aql. The theoretical Rosseland radii of the first-overtone models E and O are clearly too large compared with measured Rosseland radii. The same conclusions are also valid for the linear stellar filter radii $R_{\rm K}$ (Fig. 3).

Table 5. Measured linear Rosseland radii of R Aql for the well fitting near-maximum fundamental mode models D, P and M and comparison with theory. The model-averaged measured linear Rosseland radii are averages over those cycles of the model where the measured and theoretical linear Rosseland radius values are within the error bar. For comparison, the linear uniform disk radius of R Aql is $248^{+93}_{-56}\,R_\odot$.

model	measured linear Rosseland radius ($R_\odot$)	theoretical linear Rosseland radius ($R_\odot$)
D	258^{+99}_{-59}	246
P	242^{+99}_{-59}	263
M	250^{+97}_{-58}	315

Table 5 lists measured linear Rosseland radii of R Aql derived from the well fitting near-maximum fundamental mode models D, P and M and the corresponding theoretical ones. The model-averaged measured linear Rosseland radii are averages over those cycles of the model where the measured and theoretical linear Rosseland radius values are within the error bar (see Fig. 3).

4. Discussion

We derived angular uniform-disk diameters Θ_{UD} of five Mira stars (Table 1) from K'-band visibility measurements with the IOTA interferometer and the FLUOR beam combiner at a 38 m baseline. Using simultaneously observed bolometric fluxes and the measured uniform-disk diameters we obtained $T_{\rm eff,UD}$ values given in Table 4.

Previous interferometric K-band observations of some of our target stars (R Aql, X Oph, R Ser) were carried out by van Belle et al. (1996) at similar phases. Their derived uniform-disk diameters (R Aql; $\Phi_{\rm vis} = 0.90$: 10.76±0.61 mas, X Oph; $\Phi_{\rm vis} = 0.75$: 12.30±0.66 mas, R Ser; $\Phi_{\rm vis} = 0.32$: 8.56±0.58 mas) are in good agreement with our observations. Their effective temperatures derived from measured angular Rosseland radii (R Aql: 3189±147 K, X Oph: 3041±160 K, R Ser: 2804±144 K) are also in agreement with our results.

The comparison of the observations with Mira star models with respect to the effective temperature suggests that the four observed M Miras can approximately be

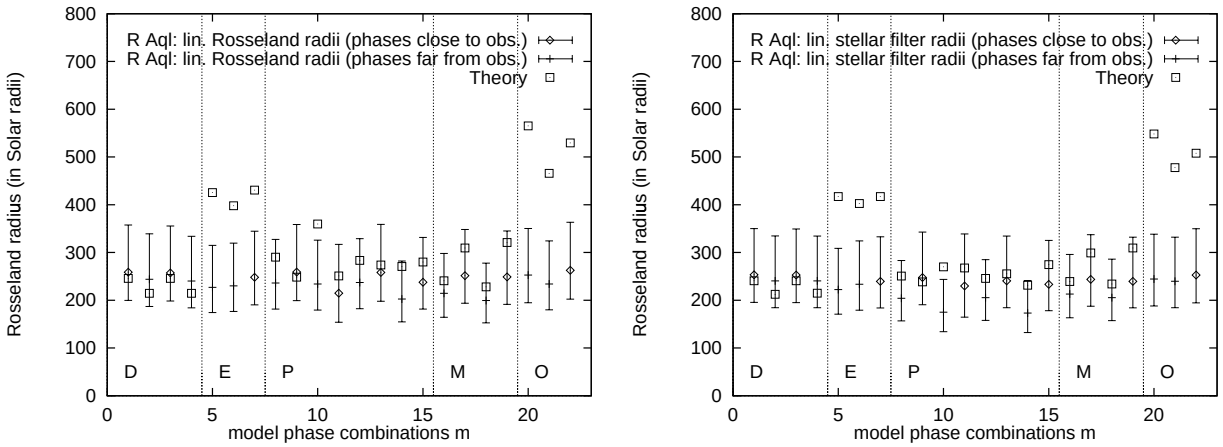

Fig. 3. Comparison of measured R Aql radii and theoretical model radii: (left) linear Rosseland radii $R_{\rm m}$ and (right) linear stellar K-band radii $R_{\rm K,m}$ for all 22 model-phase combinations m. Measured linear radii derived from models with phases close to our observations (diamonds) and far from our observations (crosses) are shown. The theoretical model radii are plotted with squares. Table 3 gives the link between the abscissa values (model-phase combinations m) and the models and their phases.

represented by the fundamental mode models D, P or M, whereas the overtone models are much too cool. For the two M stars R Aql and RU Her, phase- and model-dependent effective temperatures could be derived which are listed in Table 4. These effective temperatures are within the error bars of the $T_{\rm eff}$ values obtained with the measured uniform disk diameter. Any more accurate model interpretation of our four M-type stars would require an extension of the parameter range (Table 2) and refining the phase spacing (Table 3) of available Mira model grids. A quantitative study of V CrB can only be given on the basis of C-type Mira models which are not available yet.

For R Aql a useful HIPPARCOS parallax (4.73 ± 1.19 mas) is available and it is therefore possible to compare measured linear Rosseland and stellar K-band radii with the theoretical radii of the BSW96 and HSW98 models. The measured radii were derived by fitting theoretical (BSW96, HSW98) center-to-limb intensity variations to the visibility data. In Table 5 the measured linear Rosseland radii derived from the well fitting near-maximum fundamental mode models D, P and M are listed. From the measured linear Rosseland radii of R Aql the pulsation mode could not be determined because of the large parallax error.

The comparison suggests that R Aql can well be represented by the fundamental mode D or P model. Note, however, that observations in more filters than just one continuum filter and more baselines may be necessary for safely distinguishing a well-fitting model from an accidental match (cf. Hofmann et al. 2000). Furthermore, in order to discover the tail structure predicted by some models, future observations should cover more baselines.

Appendix A: Bolometric fluxes

The bolometric fluxes are determined by integrating the spectral energy distributions (SEDs). The present $JHKLM$ photometry were complemented by coeval V data of the AAVSO (Mattei 2001). Inspection of $BVRJ$ photometry taken one pulsational cycle later nearly at the same phase shows good agreement with the AAVSO data. From this data the R fluxes at epoch and cycle of the present observations were interpolated. Table A presents the V (AAVSO), R (interpolated) and $JHKLM$ magnitudes. In the long-wavelength regime the respective IRAS meassurements were taken into account, and in the case of R Aql also 8-30 μm photometry of Epchtein et al. (1980) taken at almost the same phase as our data ($\Phi = 0.11$). Interstellar extinction corrections, $A_{\rm V}$, are given by Whitelock & Feast (2000) and were considered by adopting the method of Savage & Mathis (1979) with $A_{\rm V} = 3.1E(B-V)$. However, extinction is generally small (see Table A) and affects the fluxes only mildly.

The $JHKLM$ photometry can be well fitted with a black body. For the fitting procedure the Levenberg-Marquardt method (see Press et al. 1992) was applied. However, these black body fits are not well suited to represent the optical and mid-infrared data (see Fig. A.1). In the optical regime the SED can be significantly depressed compared to a black body due to absorption bands (e.g. of TiO; see Scholz & Takeda 1987). For example, all oxygen-rich Mira stars of the present sample show V magnitudes well below that of a black body. To find a fair representation of the optical flux, the VRJ photometry was fitted separately applying the Levenberg-Marquardt method. Fit functions resembling black bodies but showing larger spectral indices proved to give good matches to the observational data and smooth transitions to the near-infrared photometry.

On the other hand, longwards of 10 μm dust emission may give additional, albeit small, flux contributions. For instance, the IRAS data of R Aql does not follow the Rayleigh-Jeans curve indicating the existence of possibly significant dust emission. However, we found the respective flux contributions due to dust emission to be less than

Table A.1. Pulsational phase, $\Phi_{\rm vis}$, photometric data in the V (0.55 μm, AAVSO), R (0.71 μm, interpolated), J (1.25 μm), H (1.62 μm), K (2.20 μm), L (3.50 μm), and M (4.80 μm) band (in mag), adopted extinction A_V (in mag), total bolometric flux, $F_{\rm bol}$, based on a three-component fit to the VRJ, $JHKLM$ and mid-infrared data, flux difference $\delta F_{\rm bol}^{\rm bb}$ of a SED fit based only on $JHKLM$ photometry, and flux contribution $\Delta F_{\rm bol}^{\rm dust}$ due to dust emission.

Star	$\Phi_{\rm vis}$	V	R	J	H	K	L	M	$A_{\rm V}$	$F_{\rm bol}$ [10^{-8} erg/cm^2 s]	$\delta F_{\rm bol}^{\rm bb}$	$\Delta F_{\rm bol}^{\rm dust}$
X Oph	0.71	8.30	5.43	0.55	-0.32	-0.83	-1.49	-1.25	0.18	287.7	+26.2%	2.4%
R Aql	0.17	7.90	5.01	0.47	-0.40	-0.86	-1.40	-1.32	0.23	305.6	+29.5%	1.5%
RU Her	0.07	7.70	5.12	1.28	0.53	-0.11	-0.82	-0.66	0.04	153.2	+12.9%	1.8%
R Ser	0.28	9.90	6.55	1.26	0.45	0.02	-0.51	-0.30	0.04	130.3	+40.7%	2.7%
V CrB	0.07	8.10	5.73	2.79	1.68	0.96	-0.10	-0.13	0.03	59.9	- 6.0%	2.4%

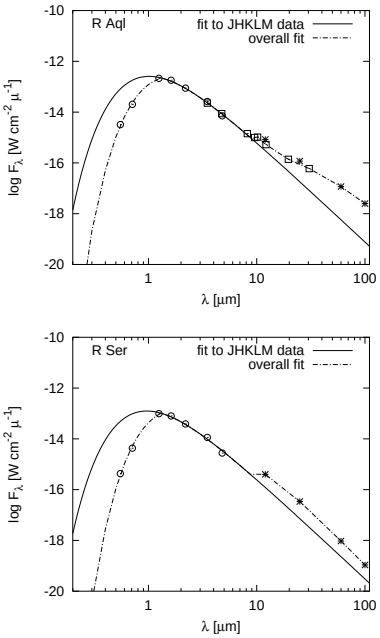

Fig. A.1. Spectral energy distributions of R Aql and R Ser. Circles refer to AAVSO data and present photometry (see Tab. A), rhombs to the photometry of Epchtein et al. (1980), and asterisks to IRAS (1985) data. The solid line represents the black-body fit to the $JHKLM$ data, and the thick dashed line refers to the overall fit.

3% (Table A), and therefore to be of only minor importance.

Table A presents the photometric data in the V (0.55 μm, AAVSO), R (0.71 μm, interpolated), J (1.25 μm), H (1.62 μm), K (2.20 μm), L (3.50 μm), and M (4.80 μm) band, the pulsational phase at date of observation, the adopted extinction, and the total bolometric flux. The flux difference of a SED fit based only on the $JHKLM$ photometry and the flux contribution due to dust emission are given as well. Fig. A.1 illustrates photometric data and various fits for R Aql and R Ser.

Acknowledgements. We thank the referee for valuable remarks. We acknowlegde usage of observations from the AAVSO international database. This research has made use of the SIMBAD database, operated by CDS in Strasbourg,

References

Bedding T., Jacob A.P., Scholz M., Wood P.R. 2001, in preparation
Bessell M.S., Brett J.M., Scholz M., Wood P.R. 1989, A&A 213, 209
Bessell M.S., Scholz M., Wood P.R. 1996, A&A 307, 481 (BSW96)
Bonneau D., Labeyrie A. 1973, ApJ 181, L1
Carleton N.P., Traub W.A., Lacasse M.G., et al. 1994, Proc. SPIE 2200, 152
Coudé du Foresto V., Ridgway S.T., Mariotti J.-M. 1997, A&AS 121, 379
Dyck H.M., Benson J.A., Van Belle G.T., Ridgway S.T. 1996, AJ 111(4), 1705
Epchtein N, Guibert J, Nguyen-Quang-Rieu, Turon P., Wamsteker W., 1980, A&A 85, L1
ESA 1997, The Hipparcos & Tycho Catalog, ESA SP-1200, Noordwijk: ESA
Fox M.W., Wood P.R. 1982, ApJ 259, 198
Haniff C.A., Scholz M., Tuthill P.G. 1995, MNRAS 276, 640
Hofmann K.-H., Scholz M., Wood P.R., 1998 A&A 339, 846 (HSW98)
Hofmann K.-H., Balega Y., Scholz M., Weigelt G. 2000, A&A 353, 1016
Hofmann K.-H., Beckmann U., Blöcker T., Coudé du Foresto V., Lacasse M., Millan-Gabet R., Morel S., Pras B., Ruilier C., Schertl D., Scholz M., Shenavrin V., Traub W., Weigelt G., Wittkowski M., Yudin B. 2000, Observations of Mira stars with the IOTA/FLUOR interferometer and comparison with Mira star models, in: *Interferometry in Optical AStronomy*, 27-29 March 2000, P.J. Lena, A. Quirrenbach (eds.), Soc. Photo-Opt. Instr. Eng., 4006, 688
IRAS, Point Source Cataloque, 1985, US Government Publication Office
Karovska M., Nisenson P., Papaliolios C., Boyle R.P. 1991, ApJ 374, L51
Mattei J.A., 2001, Observations from the AAVSO International Database, private communication
Perrin G., Coudé du Foresto V., Ridgway S.T., et al. 1998, A&A 331, 619
Perrin G., Coudé du Foresto V., Ridgway S.T., et al. 1999, A&A 345, 221
Press W.H., Teukolsky S.A., Vetterling W.T., Flannery B.P., 1992, Numerical Recipes, Cambridge University Press.
Quirrenbach A., Mozurkewich D., Armstrong J.T., et al. 1992, A&A 259, L19
Savage B.D., Mathis J.S., 1979, ARA&A 17, 73
Scholz M. 1985, A&A 145, 251
Scholz M. 2000, MNRAS, in press
Scholz M., Takeda Y. 1987, A&A 186, 200 (erratum: 196, 342)

Spinrad H., Wing R.F. 1969, ARA&A 7, 249
Traub W.A., et al. 1998, Proc. SPIE 3350, 848
Tuthill P.G., Haniff C.A., Baldwin J.E. 1995, MNRAS 277, 1541
Van Belle G.T., Dyck H.M., Benson J.A., Lacasse M.G. 1996, AJ 112, 2147
Van Leeuwen F., Feast M.W., Whitelock P.A., Yudin B. 1997, MNRAS 287, 955
Watanabe T., Kodaira K. 1979, PASJ 31, 61
Whitelock P, Feast M., 2000, MNRAS 319, 759
Weigelt G., Balega Y., Hofmann K.-H., Scholz M. 1996, A&A 316, L21